



## OPEN The pathomechanism of bone marrow edema in the femoral head necrosis with pericollapse stage

Liang Mo<sup>1,2</sup>, Zhangzheng Wang<sup>1,2</sup>, Mengyu Jiang<sup>1,2</sup>, Chi Zhou<sup>1,2</sup>, Chao Ma<sup>2</sup>, YINUO Fan<sup>2</sup>, Wei He<sup>1,2</sup>✉, Zhenqiu Chen<sup>1,2</sup>✉ & Yuhao Liu<sup>1,2</sup>✉

Bone marrow edema (BME), a notable manifestation during the progression of osteonecrosis of the femoral head (ONFH), exhibits significant associations with femoral head collapse, pain, and prognosis, however its pathogenesis remains underexplored. In this study, specimens from patients undergoing total hip arthroplasty (THA) were analyzed. The results revealed significantly higher Visual Analog Scale (VAS) scores and CT low-density area ratio in the BME group compared to the control group. Furthermore, Sirius Red staining exhibited fibrotic tissue in both necrotic and sclerotic areas, with more pronounced effects in the BME group. Meanwhile, data-independent Acquisition (DIA) proteomics technology was utilized to identify differentially expressed proteins (DEPs) within bone tissue. 141, 299 and 852 DEPs were identified in femoral neck, necrotic and sclerotic regions, respectively. Immune responses, inflammatory reactions and oxidative stress were markedly altered in ONFH cases with BME. In bone tissue, the levels of malondialdehyde (MDA) and proteins associated with osteoclast activity were found to be elevated in the BME group. In conclusion, BME in ONFH at pericollapse stage is associated with inflammation, fibrosis, heightened oxidative stress and increased osteoclast activity. These factors collectively elevated the risk of collapse or re-collapse. Targeted interventions aimed at neutralizing these risk factors show potential in slowing down the progression of the disease.

**Keywords** Osteonecrosis of the femoral head, Bone marrow edema, Osteoclast, Inflammation, Oxidative stress

### Abbreviations

ONFH	Osteonecrosis of the femoral head
BME	Bone marrow edema
THA	Total hip arthroplasty
MRI	Magnetic resonance imaging
DIA	Data-independent Acquisition
MDA	Malondialdehyde
VAS	Visual Analog Scale
DEPs	Differentially expressed proteins
ARCO	Association for Research on Osseous Circulation
PBS	Phosphate-buffered saline
HE	Hematoxylin-eosin
ROI	Region of interest
ROS	Reactive oxygen species

Osteonecrosis of the femoral head (ONFH) is a refractory and debilitating bone disease that commonly affects young and middle-aged individuals. Trauma, corticosteroid use, and excessive alcohol consumption are its primary risk factors<sup>1</sup>. In recent decades, ONFH has garnered substantial attention from researchers. However, a consensus on the precise pathogenesis has not yet been reached. Nevertheless, existing studies indicate that regardless of different risk factors and underlying conditions, ONFH arises from compromised blood supply to the femoral head, leading to necrosis of the bone marrow. Subsequent stress on the affected area can result in

<sup>1</sup>The First Affiliated Hospital of Guangzhou University of Chinese Medicine / Guangdong Clinical Research Academy of Chinese Medicine, Guangzhou, China. <sup>2</sup>Present address: Guangzhou University of Chinese Medicine, Guangzhou, China. ✉email: hw13802516062@163.com; chenchenqiu2012@126.com; doctor\_yuhaoliu@126.com

subchondral fractures and collapse of the joint<sup>2</sup>. Total hip arthroplasty (THA) is currently an effective treatment for end-stage ONFH. However, for young and middle-aged patients, there are long-term concerns such as prosthetic failure associated with joint replacement<sup>3,4</sup>. Therefore, hip preservation treatments, which aim to salvage the patient's own hip joints, are of significant clinical and societal value.

The selection of patients is of utmost importance in determining the success rate of treatments for hip preservation<sup>5,6</sup>. To better guide the diagnosis and treatment of ONFH, researchers have put forward a novel definition of the peri-collapse stage of ONFH, which is characterized by the presence of a subchondral fracture and continues until the collapse of the femoral head exceeds 2 mm<sup>7</sup>. Bone marrow edema (BME) is a diffuse and ill-defined abnormality in the femoral head and neck and is a typical radiographic manifestation during the peri-collapse stage of ONFH<sup>7</sup>. It appears as decreased signal intensity on magnetic resonance imaging (MRI) T1-weighted images and increased signal intensity on MRI T2-weighted images, which can be attributed to elevated levels of free water or hemorrhage within the bone marrow<sup>8</sup>. With the widespread use of MRI in clinical practice, it has been observed that BME frequently accompanies ONFH and is closely associated with the progression of the disease<sup>9</sup>. Meier et al.<sup>10</sup> reported that BME of the femoral head in ONFH patients represents a secondary sign of subchondral fracture and thus indicates stage 3 disease according to the Association for Research on Osseous Circulation (ARCO). Another study has also confirmed this conclusion<sup>11</sup>. However, current research predominantly focuses on exploring the correlation among BME, femoral head collapse, and pain, with limited investigation on the underlying pathological mechanisms.

Understanding the pathological mechanisms of ONFH with BME is particularly important for selecting hip preservation treatments during the peri-collapse stage. Therefore, to better investigate the potential mechanisms, the histopathological characteristics between BME and non-BME bone tissues were compared. Furthermore, we conducted a data-independent acquisition (DIA) based quantitative proteomics analysis of BME and control bone tissues, including femoral neck, necrotic and sclerotic regions. The results of this study may give new insight into the molecular basis of the pathogenesis in ONFH accompanied BME and provide novel clues for the treatment of ONFH during the peri-collapse stage.

## Materials and methods

### Study population

This study was approved by the Ethical Committee of the First Affiliated Hospital of Guangzhou University of Chinese Medicine (No. K-2022-059). The research was performed in accordance with the Declaration of Helsinki and relevant guidelines, all patients provided written informed consent to participate in the research. Patients who were diagnosed with ONFH caused by excessive glucocorticoid use or alcohol abuse, and were scheduled for THA were recruited. The imaging data (X-ray, MRI, CT) of all the included patients were independently assessed by two radiologists.

The diagnostic criteria for BME were consistent with earlier research<sup>10</sup>, manifesting as reduced signal intensity on T1-weighted images and heightened signal intensity on T2-weighted images. The severity of BME was classified based on the extent of edema affecting either the femoral head only (1-degree, minimal), both the femoral head and neck (2-degree, moderate), or extending to the intertrochanteric region (3-degree, extensive).

### Inclusion and exclusion criteria

Patients were selected based on the following inclusion criteria: (1) Those diagnosed with ONFH at the peri-collapse stage<sup>7</sup>, or ARCO stages II and IIIA (collapse < 2 mm) according to the 2019 revised ARCO staging system<sup>12</sup>; (2) Age range between 18 and 55 years; (3) Availability of preoperative imaging data (X-ray, CT, and MRI) within one week before THA. Patients were excluded if they met any of the following criteria: (1) History of traumatic hip injury or other bone metabolism diseases; (2) Previous hip preservation surgeries, such as bone grafts or core decompression; (3) Use of hormonal medications or anti-osteoporosis drugs within three months prior to THA; (4) Presence of severe cardio-cerebral diseases, renal, or hematological conditions. Ultimately, only five patients with 3-degree BME (MRI revealed diffuse concomitant BME at the femoral neck, intertrochanteric and trochanteric regions) were included in the study, and five ONFH patients with 0-degree BME were selected as the control group.

### Human femoral head specimen harvest

Consent was obtained from the patients prior to obtaining femoral head specimens during THA surgery. Using a bone tissue pathological cutting machine (EXAKT312), each specimen was sliced in coronal sections of 5 mm thickness. Subsequently, both the bone slices were stored at  $-80^{\circ}\text{C}$  for further analysis.

### Hematoxylin-eosin and sirius red staining

The bone slice near the center of the femoral head was selected for subsequent histology. After fixing the tissues in 4% formaldehyde for at least 24 h at room temperature and clearing in phosphate-buffered saline (PBS), the samples were decalcified with 10% EDTA for at least 4 weeks. A sterile bone cutter was used to cut the bone slice into small regions (encompassing the necrotic, sclerotic, and femoral neck regions), which were embedded in paraffin wax after being dehydrated an automatic tissue dehydrator (Leica TP1020). Specimens were cut into 5- $\mu\text{m}$  sections (Leica 2135, Wetzlar, Germany) and stained with hematoxylin-eosin (HE) and Sirius Red. Images were observed and captured using a microscope (BX53, Olympus Corp., Tokyo, Japan). Then, the images of HE and Sirius Red staining from each sample were used to evaluate the bone trabecular morphology, ratio of empty lacunae (empty lacunae/total lacunae) and the degree of bone tissue fibrosis.

Furthermore, we observed that patients in the BME group had a higher probability of low-density changes on CT (100% in this study). Consequently, five representative sections close to the midpoint were extracted from

the patients' CT imaging data, and quantitative analysis of the CT low-density area ratio was carried out using ImageJ software.

### Bone tissue protein extraction and enzymatic hydrolysis

Protein extraction was carried out from three non-BME femoral head and three BME femoral head bone tissue samples. (1) Different regions (femoral neck, necrotic and sclerotic regions) were extracted from each bone slice samples near the center of the femoral head with a sterile blade; (2) The bone samples were ground in liquid nitrogen and the sample power was transferred into a 5 ml EP tube; (3) 500  $\mu$ l LSDT protein lysate (4% SDS, 100 mM Tris-HCl, 100 mM DTT, pH 8.0) was added<sup>13</sup>; (4) The mixture was boiled for 5 min, homogenized by ultrasound (25 W, ultrasound 3 s, interval 7 s) in ice bath for 5 min, and centrifuged at 14,000 g for 30 min. The supernatant was filtered with 0.22  $\mu$ m ultrafiltration device (Corning, NY, USA) and stored at  $-80^{\circ}\text{C}$ . (5) Protein content was quantified by BCA protein assay reagent (Bio-Rad, CA, USA) and the quality was examined by SDS-PAGE.

Protein enzymatic hydrolysis was performed as follows: (1) Take 100  $\mu$ g of protein solution per sample and dilute with 50mM  $\text{NH}_4\text{HCO}_3$  by 4-fold volumes; (2) Add 2.5  $\mu$ g of Trypsin enzyme in the ratio of protein: enzyme = 40:1, and digest for 4 h at  $37^{\circ}\text{C}$ ; (3) Enzymatic peptides were desalted using a Strata X column and vacuumed to dryness.

### High pH RP separation

Equal amounts of peptides were extracted from all samples and combined to form a mixture. The mixture was then diluted with mobile phase A (5% ACN pH 9.8) and injected into a Shimadzu LC-20AB HPLC system coupled with a Gemini high pH C18 column (5  $\mu$ m,  $4.6 \times 250$  mm). The sample was subjected to column separation and eluted at a flow rate of 1 mL/min using a gradient elution method. The elution gradient consisted of 10 min at 5% mobile phase B (95% ACN, pH 9.8), followed by a 40-minute increase from 5 to 35% mobile phase B, a 1-minute increase from 35 to 95% mobile phase B, a 3-minute flow of mobile phase B, and finally a re-equilibration at 5% mobile phase B for 10 min. During the elution process, the absorbance of the elution peak was monitored at a wavelength of 214 nm, and the eluted components were collected every minute. The collected components were combined into a total of 10 fractions, which were subsequently subjected to freeze-drying.

### LC-MS/MS analysis

The dried peptide samples were reconstituted with mobile phase A (100% H<sub>2</sub>O, 0.1% FA), centrifuged at 20,000 g for 10 min, and the supernatant was taken for injection. Separation was performed by Bruker Nano Elute. The sample was first enriched in the trap column and desalted, and then entered a tandem self-packed C18 column (75  $\mu$ m internal diameter, 1.8  $\mu$ m column size, 25 cm column length), and separated at a flow rate of 300 nL/min by the following effective gradient: 10 min, 2% mobile phase B (100% ACN, 0.1% FA); 10 ~ 45 min, mobile phase B linearly increased from 2 to 22%; 45 ~ 50 min, mobile phase B rose from 25 to 35%; 50 ~ 55 min, mobile phase B rose from 35 to 80%; 55 ~ 60 min, 80% mobile phase B. The nanoliter LC separation end was directly connected to the mass spectrometer and detected according to the following parameters:

The peptides separated by liquid phase chromatography were ionized by a nanomesa source and then passed to a tandem mass spectrometer timsTOF Pro for DDA (Data Dependent Acquisition) mode detection. The main parameters were set: ion source voltage was set to 1.6 kV, ion mobility range was 0.6–1.60 V.S/cm<sup>2</sup>; MS1 mass spectrometer scanning range was 302 ~ 1,077 m/z and the peak intensity above 2500 can be detected; The 302 ~ 1,077 m/z was divided into 4 steps, and each step was divided into 8 Windows. A total of 32 Windows was used for continuous window fragmentation and information collection. The fragmentation mode was CID, the fragmentation energy was 10 eV, and the mass width of each window was 25. The cycle time of a DIA scan was 3.3 s.

### Bioinformatic analysis

This process is based on the sample data generated from a high-resolution mass spectrometer. For large-scale DIA data, prophet algorithm was used to complete analytical quality control, thus obtaining many reliable quantitative results. The database used was uniprot\_reviewed\_human\_2020081\_1\_20396.fasta (total 20,396 sequences). The DIA data was analyzed using the iRT peptides for retention time calibration. Then, based on the target-decoy model applicable to SWATH-MS, false positive control was performed with FDR 1%, therefore obtaining significant quantitative results. MSstats<sup>14</sup> screened DEPs according to a difference multiple  $\geq 1.5$  and  $p < 0.05$  as the criteria for determining significant difference.

Principal Component Analysis (PCA) was employed to assess the homogeneity within groups and heterogeneity between groups. Additionally, to decipher the functional attributes of the identified proteins, the DEPs were subjected to enrichment analysis using the Metascape database (<http://metascape.org/>). Furthermore, protein-protein interaction (PPI) networks were constructed utilizing the STRING database (<http://string.embl.de>) and visualized using the Cytoscape web application (Version 1.0.4, <http://www.cytoscape.org>).

### Malondialdehyde (MDA) analysis

Bone tissue samples from five BME and control patients were taken as the study objects. MDA was calculated using the MDA assay kit (Beyotime, China). The extraction solution was added according to the instructions of the manufacturer's instructions, and after ultrasonic crushing, centrifugation, and taking the supernatant. The absorbance of the supernatant was measured by a spectrophotometric assay at 532 nm for MDA.

## Western blot

Protein samples were separated using 12% SDS-PAGE and subsequently transferred onto PVDF membranes (Millipore). The membranes were then blocked with 3% bovine serum albumin (BSA) in TBST for 2 h at room temperature. Following blocking, the membranes were incubated with antibodies specific to CTSK, SOD-1 and RANKL (Santa cruz, America). Human GAPDH was used as a marker for quantification. Enhanced chemiluminescence (ECL) western blot detection system was utilized for semi-quantitative analysis and visualization of the specific proteins. The intensities of protein bands were calculated by comparing them relative to GAPDH for each sample.

## Statistical analysis

The data analysis for this study was conducted using GraphPad Prism version 8.0 software. Quantitative results that followed a normal distribution were summarized as mean  $\pm$  standard deviation. For comparing two independent sample groups, we applied parametric tests. Specifically, Student's t-test was used for data with equal variances, while the *Mann-Whitney U* test was employed for non-normally distributed data. When comparing multiple sample groups, one-way analysis of variance (ANOVA) was utilized for normally distributed datasets. Additionally, to gain a better understanding of the magnitude and importance of the observed differences, effect sizes were calculated. The semi-quantification of CT low-density areas and Sirius Red-stained images was performed using ImageJ software. A p-value less than 0.05 was considered statistically significant.

## Results

### Demography of cases in the two groups

A lower occurrence of severe BME was observed in patients during the perioperative period in this study. Those with significant joint collapse or advanced osteoarthritis had either a reduced incidence or no signs of severe BME. Following the established inclusion and exclusion criteria, only five ONFH patients displayed grade 3-degree BME on MRI scans conducted within a week prior to their THA surgeries. The BME manifestation was primarily concentrated in the head-neck and trochanteric areas. To ensure a controlled environment, a selection of five peri-collapse stage ONFH patients, presenting with grade 0 BME, were chosen as a matched control group, based on factors such as etiology, age, gender and staging criteria. Consequently, a total of ten femoral head specimens were acquired from THA patients, consisting of seven males and three females. The findings indicated a marked elevation in Visual Analog Scale (VAS) scores among individuals with BME, as opposed to the control group (Table 1).

### Imaging data and histomorphometry analysis

Macroscopic observations of the two groups of femoral head specimens are as follows: The articular surface of the femoral head in the weightbearing area lacked fullness, with the joint cartilage displaying a white hue and a glossy sheen, maintaining uniform thickness. Beneath the weightbearing area, the joint soft tissues comprised the necrotic zone, which exhibited a pale gray or light-yellow color, free from luster, and contained irregular translucent bands areas of bone resorption and defects. The trabeculae were disorganized, and the bone was sparse. Below the necrotic zone lied the sclerosis zone, characterized by a grayish tone, dense and rigid bone tissue. Furthermore, cystic granulation tissue could be found adjacent to the sclerosis area, appearing in shades of pale yellow or dark red, having a soft texture. Below the sclerosis zone was the normal zone bone tissue, showcasing a fresh pale-yellow color, well aligned trabeculae, and a moderate level of hardness.

The imaging results showed that in the BME group, the femoral head exhibited diffuse high signal intensity on T2-weighted images in the head-neck and trochanteric regions. Additionally, there were evident low-density shadows observed on X-ray frog-leg views (Fig. 1A). On femoral head sections, subchondral fractures and collapse could be observed (Fig. 1C). However, this phenomenon was not observed in control group (Fig. 1B and D). These findings suggested that the presence of BME is associated with structural changes in the femoral head, including subchondral fractures and collapse.

Group/ Patient ID	Age (years)	Gender	Etiology	BME degree*	VAS scores*	Harris scores	DIA
BME group	1 43	Male	Glucocorticoid	3	7	65	√
	2 30	Male	Glucocorticoid	3	7	45	√
	3 30	Male	Alcohol	3	8	54	-
	4 41	Female	Glucocorticoid	3	7	54	√
	5 35	Male	Alcohol	3	7	43	-
Non-BME group	6 35	Male	Alcohol	0	5	65	-
	7 35	Female	Glucocorticoid	0	2	60	√
	8 27	Female	Glucocorticoid	0	3	48	√
	9 35	Male	Glucocorticoid	0	4	65	√
	10 34	Male	Alcohol	0	3	52	-

**Table 1.** Basic characteristics of the study subjects. VAS, Visual Analog Scale; DIA: Data-independent acquisition;  $P_{\text{Age}}=0.429$ ,  $P_{\text{Gender}}=0.197$ ,  $P_{\text{Etiology}}=1$ ,  $P_{\text{BME}} < 0.001$ ,  $P_{\text{Harris}}=0.299$ ,  $P_{\text{VAS}} < 0.001$ .

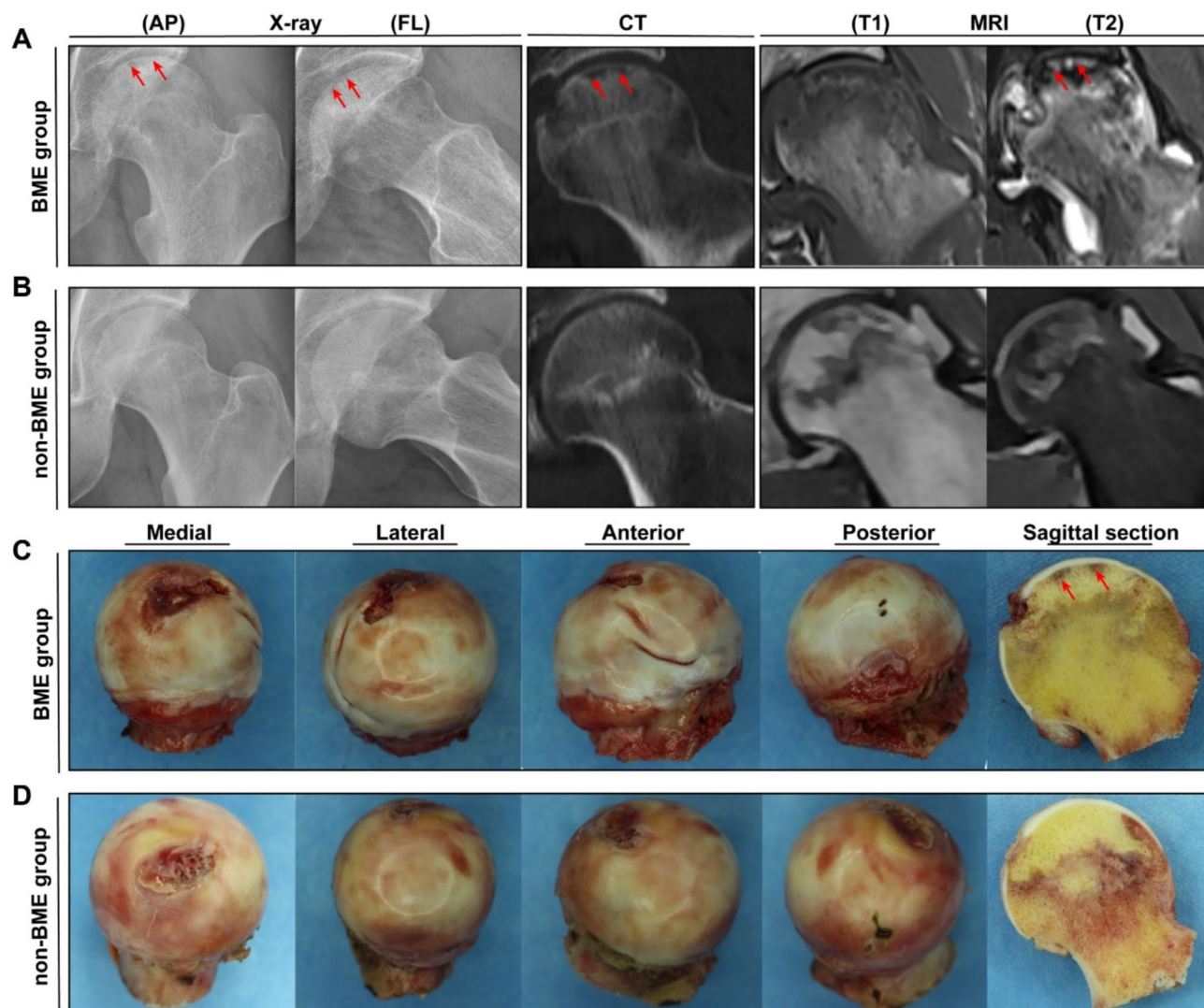


**Fig. 1.** Representative imaging (including X-ray, CT and MRI) and photographs of the femoral heads from BME group and control group patients with ONFH. Imaging data of BME group (A) and control group (B). Femoral heads gross sample pictures of BME group (C) and control group (D). Red arrows represented subchondral fracture.

### Hematoxylin-eosin, sirius red staining and CT low-density area ratio measurement

Figure 2A–B presented the HE staining results, which demonstrated the presence of evident bone resorption and cystic changes in the histological sections of the BME group. In both groups of patients, the rate of empty lacunae in the necrotic area was significantly higher than in the normal and sclerotic areas. Additionally, the rate of empty lacunae in the sclerotic area was higher than in the control area (Fig. 2C–D). However, when comparing the rates of empty lacunae between the two groups in the control, necrotic, and sclerotic areas, no significant differences were observed (Fig. 2E). This indicated that BME is not an extension of the area affected by bone necrosis.

Tissue fibrosis occurs due to chronic inflammation, disrupting the normal processes of tissue regeneration and repair. Sirius Red staining results indicated the presence of fibrotic tissue in both necrotic and sclerotic regions. A significantly higher fibrotic response was observed in the BME group when compared to the control group (Fig. 2F–G). Upon histological examination, it was apparent that the BME group exhibited a prominent presence of granulation tissue. This tissue was rich in collagen fibers, as evidenced by Sirius Red staining. Additionally, HE staining showed that the granulation tissue was infiltrated by numerous spindle-shaped fibroblasts and inflammatory cells (Fig. 2H). Concurrently, histological analysis revealed a larger area stained positive for Sirius Red in the BME group as opposed to the control group (Fig. 2I).

Furthermore, we commonly observed low-density shadows on CT scans in BME group. The presence of these low-density areas on CT scans typically signals extensive bone destruction and marked reduction in bone mass within those specific regions. To further investigate this observation, we conducted a quantitative assessment to determine the ratio of low-density areas to the entire volume of the femoral head. Our findings notably

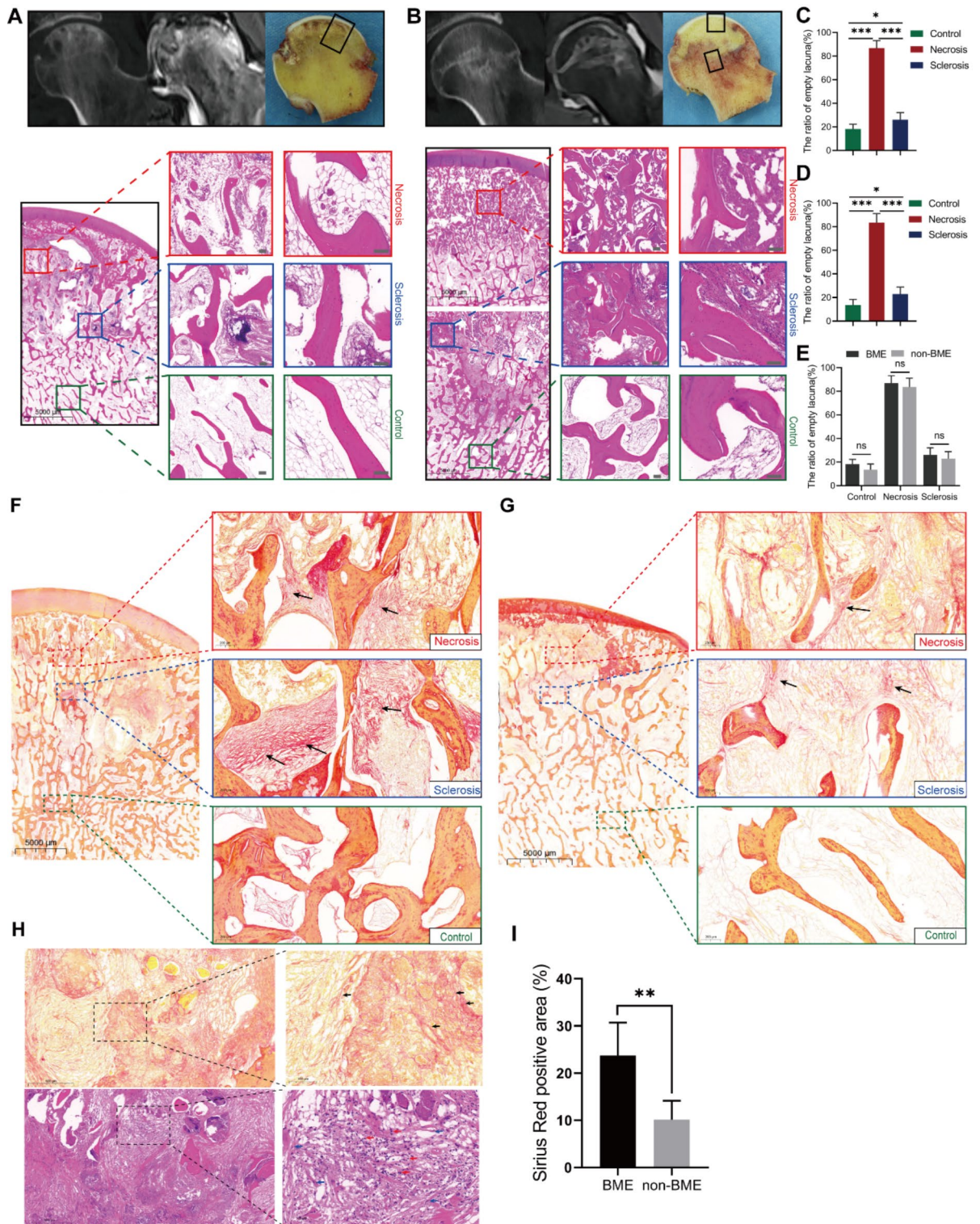


**Fig. 2.** Pathological detection results from BME and control group patients with ONFH. Representative images of HE-stained sections from patients with BME (A) and without BME (B). Scale bar = 200  $\mu$ m. The empty lacuna ratio quantification in necrotic, sclerotic and control regions from patients with BME(C) and without BME (D). (The “control” represented areas on the slice not affected by necrosis). The comparison of the empty lacuna ratio between BME group and control group (E).  $n = 5$  for each group. Sirius Red staining results from BME (F) and non-BME group (G) patients with ONFH. (H) Sirius Red and HE Staining results of granulation tissue. Black arrows represented fibrous tissue. Green arrows represented fibroblasts and red arrows represented inflammatory cells. (I) Quantification of Sirius Red positive area.  $n = 5$  for each group. \* $p < 0.05$ ; \*\* $p < 0.01$ ; \*\*\* $p < 0.001$ .

demonstrated that the prevalence of low-density regions was considerably greater in the BME group when compared to the control group (Fig. 3A-B).

### Differentially expressed proteins (DEPs) identification

The mass spectrometry proteomics data have been deposited to the ProteomeXchange Consortium (<https://proteomecentral.proteomexchange.org>) via the iProX partner repository<sup>15,16</sup> with the dataset identifier PXD048708. Based on MRI imaging data of patients, bone tissues were extracted from necrotic, sclerotic, and healthy regions in both the BME and control groups (Fig. 4A). The technical workflow for DIA proteomics analysis of bone tissue is presented in Fig. 4B. Proteins were quantified using the MSstats software package, and the resulting protein expression of each sample and relative expression between two groups were presented in the form of heatmaps (Fig. 4D and F). The quantity of peptides and proteins identified from each sample were shown in Table S1, and Fig. 4C showed the identified protein count in each sample. MSstats package was used to screen the DEPs between BME and control groups, and the screening standard was  $|\log_2FC| \geq 1.5$  and  $p$  value  $< 0.05$ . For healthy region, a total of 141 DEPs were identified, including 15 upregulated proteins and 129 downregulated proteins. For necrotic region, a total of 299 DEPs were identified, including 18 upregulated proteins and 281 downregulated proteins. For sclerotic region, a total of 852 DEPs were identified, including 779 upregulated proteins and 73 downregulated proteins (Fig. 4E). These results showed that the highest number of DEPs was found in sclerotic region, which suggested that the BME has the greatest effect on bone sclerotic region.

### Enrichment analysis and PPI network construction

To further investigate the functional enrichment of the DEPs in terms of their biological significance, Metascape, an online tool was employed to perform Gene Ontology (GO) and Kyoto Encyclopedia of Genes and Genomes (KEGG) enrichment analysis. Additionally, PPI network was conducted using the STRING database. For visualization purposes, the Cytoscape software was employed to generate a visual representation of the PPI network. The analysis revealed that the majority of differentially expressed proteins in the control region were downregulated. These proteins were primarily enriched in pathways related to immune response, cell activation, and blood coagulation (Table S2). By constructing a PPI network, it identified key modules comprising proteins such as CYBB, IL18, TLR8, WAS, and FN1 (Fig. 5A-D). These proteins played crucial roles in the aforementioned pathways, suggesting their involvement in the regulation of immune response, cell activation and blood coagulation processes.

Most of the DEPs in the necrotic region were downregulated, which were primarily enriched in pathways such as blood microparticles, proteasomes, immunoglobulin complexes and oxidoreductase activity (Table S3). By constructing a PPI network, core modules consisting of proteins such as PSMB1, BLMH, PSMA7, and CUL3 were identified (Fig. 5E-H). The number of DEPs in the sclerotic region significantly increased compared to the normal and necrotic regions. Approximately 90% of these DEPs were upregulated. Enrichment analysis revealed that the main enriched pathways include oxidoreductase activity, mitochondrial matrix, organic acid catabolic process and immunoglobulin complex (Table S4). The core modules in the PPI network consisted of proteins

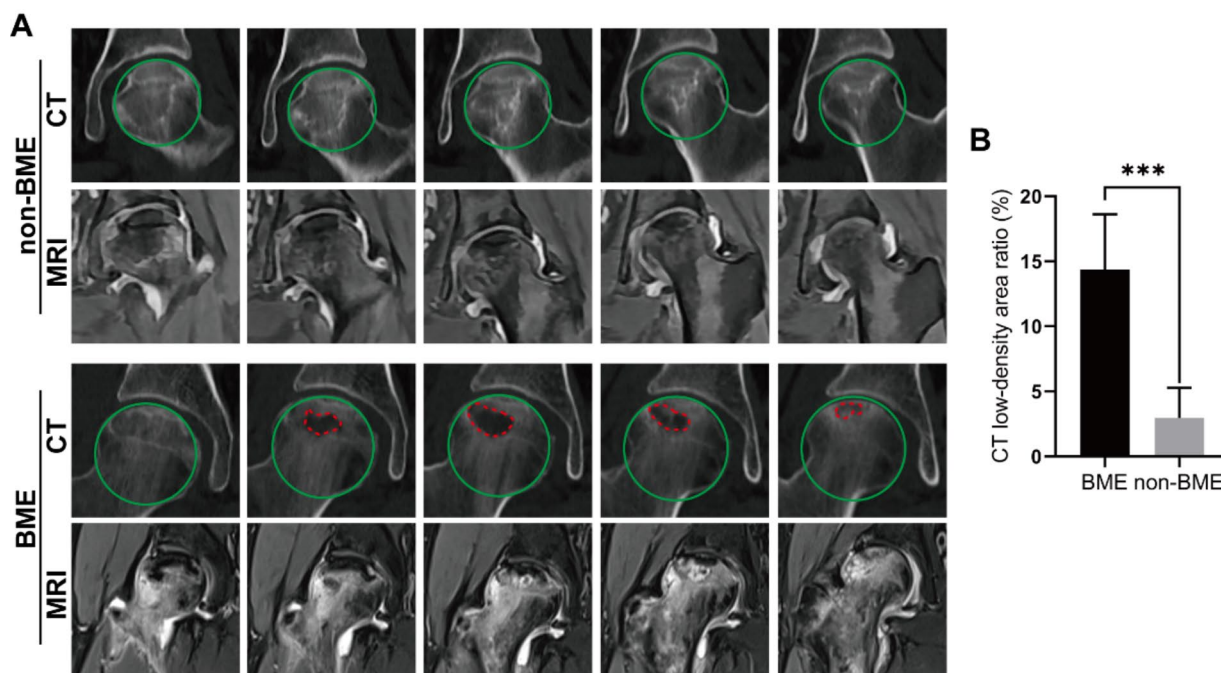


**Fig. 3.** Analysis of CT low-density area between BME and control groups. (A) CT and MRI imaging of typical case. Green circles represented the area of the femoral head, while red regions indicated the area of low-density shadows on the CT scan. (B) Quantification of CT low-density area ratio.  $n = 25$  for each group,  $***p < 0.001$ .

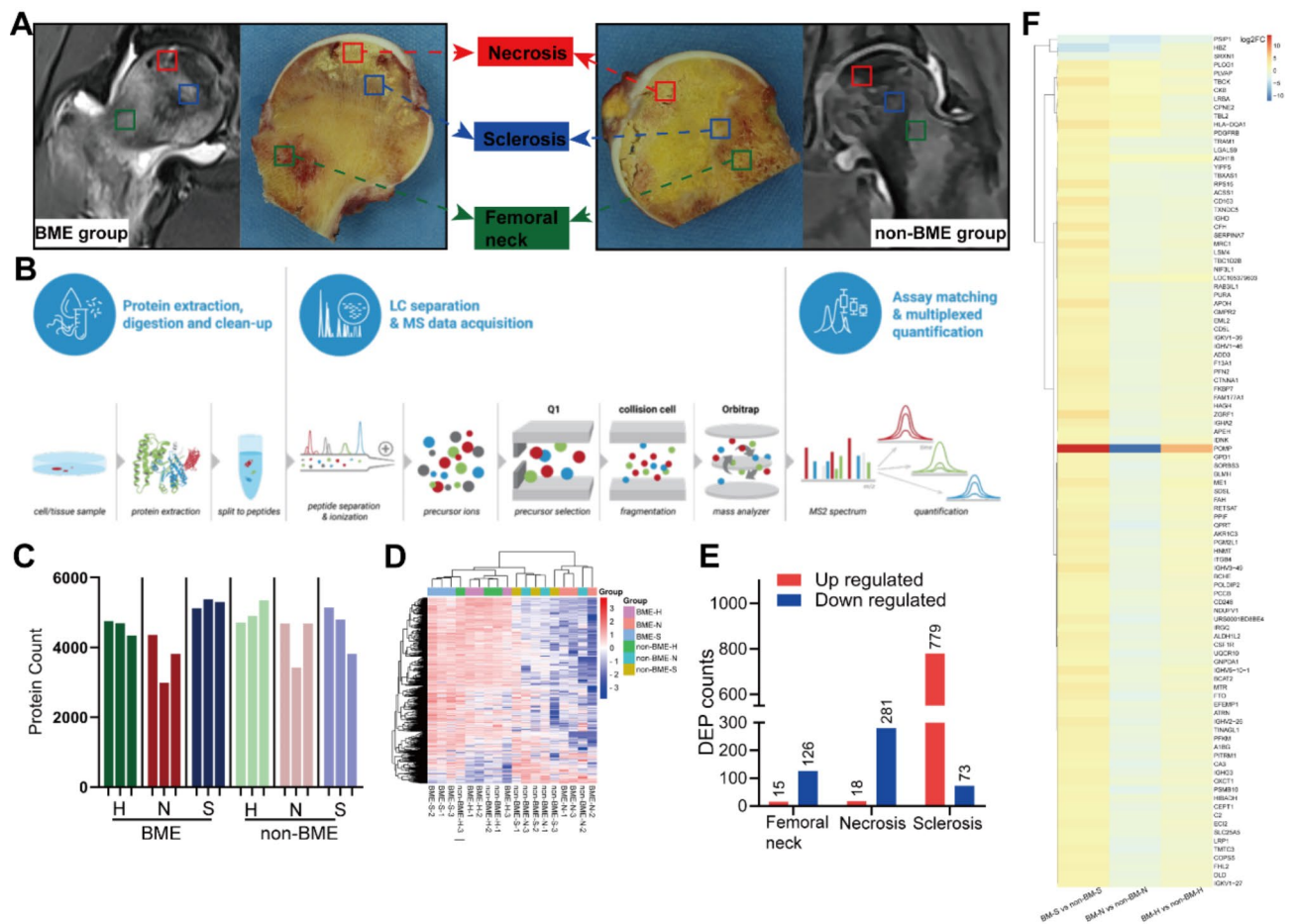


**Fig. 4.** Identification of DEPs in BME and control groups patients with ONFH using DIA proteomics technology. **(A)** Diagram of bone tissue sample extraction; **(B)** The technical workflow for DIA proteomics analysis. **(C)** Distribution of the identified proteins in individual samples; **(D)** The heatmap plot of partial DEPs expressed in different samples. **(E)** The number of DEPs identified in the same region between the two groups.  $P$  value  $< 0.05$  and  $|\log_2FC| \geq 1.5$  were selected as screening conditions; **(F)** Heatmap of DEPs between BME and control groups. H, femoral neck (control) region; N, necrosis region; S, sclerosis region; BME, bone marrow edema; non-BME, non- bone marrow edema.

such as PDHA1, ACAA1, GCDH and OXCT1(Fig. 5I-L). Additionally, top significant 10 DEPs in three regions were separately shown in Tables 2, 3 and 4.

**Quantitative of inflammatory cells and western blot analysis**

The functional enrichment analysis of DEPs in DIA proteomics revealed significant functional disparities between the BME group and the control group. These differences were mainly linked to immune responses, inflammatory reactions, and oxidative stress. To further investigate these findings, a quantitative analysis of inflammatory cells was performed on HE-stained histological sections across various regions of the bone tissue. Following HE staining, the nuclei of inflammatory cells exhibited a striking blue hue due to hematoxylin staining. Meanwhile, the cytoplasm displayed a range of colors from light pink to peach, with eosinophilic granules distinctly appearing as vivid red spots. The analysis demonstrated that inflammatory cells are mostly concentrated in the sclerosis zone in both groups. However, a comparison between the groups showed a considerably higher number of inflammatory cells in the BME group compared to the control group (Fig. 6A). The sclerotic region exhibited the highest number of DEPs, with a significantly greater quantity of inflammatory cells compared to the healthy region and necrotic region. Therefore, GSEA analysis was conducted on the overall expressed proteins in the sclerotic regions of both groups. The results indicated that these proteins were mainly enriched in immune response, organic acid metabolic processes, and oxidoreductase activity (Fig. 6B).

The sclerotic region displayed the greatest number of DEPs, with a significantly higher concentration of inflammatory cells than in the femoral neck and necrotic regions. Consequently, we performed gene set enrichment analysis (GSEA) on all expressed proteins within the sclerotic areas of both groups. Our findings showed that these proteins were primarily enriched in immune response, organic acid metabolic processes, and oxidoreductase activity (Fig. 6B). Furthermore, we assessed the levels of MDA in the bone tissue. The results indicated that MDA levels were higher in the sclerotic regions of the BME group when compared to the control



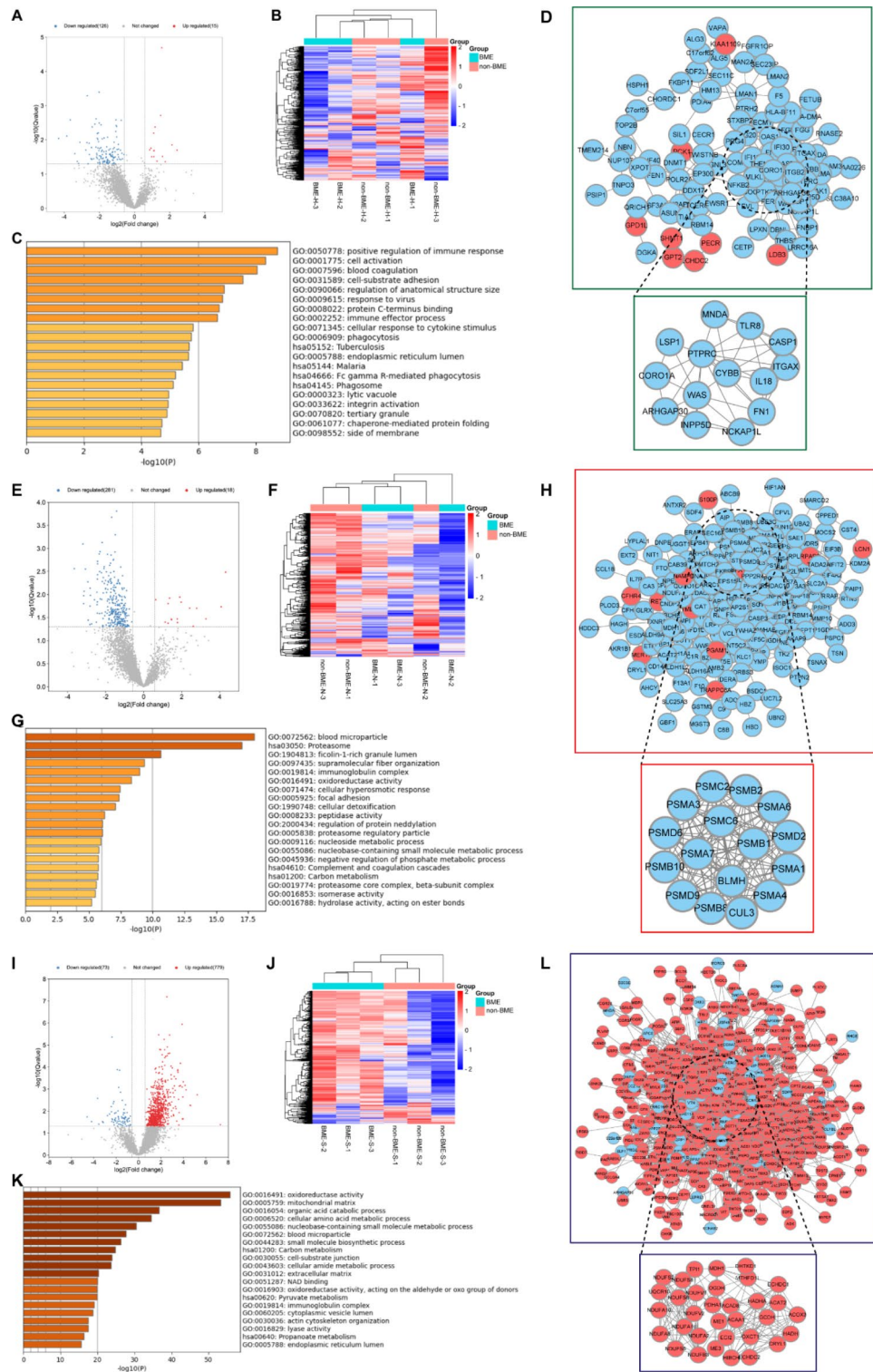


**Fig. 5.** Analysis of DEPs between BME group and non-BME groups. (A) A volcano plot of DEPs in femoral neck region. (B) A heat map of DEPs in different samples. (C) Enrichment analysis of DEPs in healthy region. (D) PPI network of DEPs in femoral neck region. (E) A volcano plot of DEPs in necrotic region. (F) A heat map of DEPs in different samples. (G) Enrichment analysis of DEPs in necrotic region. (H) PPI network of DEPs in necrotic region. (I) A volcano plot of DEPs in sclerotic region. (J) A heat map of DEPs in different samples. (K) Enrichment analysis of DEPs in sclerotic region. (L) PPI network of DEPs in sclerotic region. In the volcano map and PPI network map, red represented up-regulated and blue represented down-regulated.

Up-regulated DEPs				Down-regulated DEPs			
ID	Gene name	LogFC	Pvalue	ID	Gene name	LogFC	Pvalue
P0CG29	GSTT2B	1.104418	0.030756	P10153	RNASE2	-4.3187	0.009128
Q9BY49	PECR	1.122082	0.020492	P03951	F11	-3.8564	0.00769
O75112	LDB3	1.173369	0.004215	Q92954	PRG4	-3.6542	0.002612
Q8N335	GPD1L	1.282336	0.041916	Q8IY34	SLC15A3	-3.398	0.025036
Q86YB7	ECHDC2	1.490047	0.00193	Q9H173	SIL1	-3.2531	0.042669
Q9Y2Z9	COQ6	1.552572	2.04E-05	P00973	OAS1	-3.1785	0.048781
Q8TD30	GPT2	1.589132	0.030447	Q9UGM5	FETUB	-3.1078	0.011761
Q2LD37	KIAA1109	1.745848	0.043293	Q96AZ6	ISG20	-2.7677	0.019848
P35558	PCK1	2.131811	0.014029	P13284	IFI30	-2.7011	0.01197
O94766	B3GAT3	2.422187	0.019971	P49815	TSC2	-2.6858	0.00051

**Table 2.** Top 10 DEPs in femoral neck region between BME group and non-BME group.

Up-regulated DEPs				Down-regulated DEPs			
ID	Gene name	LogFC	Pvalue	ID	Gene name	LogFC	Pvalue
P07814	EPRS1	1.769032	0.033873	O75475	PSIP1	-3.64738	0.002744
P25940	COL5A3	1.776756	0.04046	O15027	SEC16A	-3.19435	0.0008
P50851	LRBA	1.895755	0.011344	P41159	LEP	-3.15808	0.015756
A6NHR9	SMCHD1	1.967138	0.014606	P14923	JUP	-3.15201	0.010619
O75865	TRAPPC6A	2.417621	0.019781	Q7RTS9	DYM	-3.13086	0.008518
Q9HD89	RETN	2.60276	0.048799	P09913	IFIT2	-3.0629	0.002806
Q9BVQ7	SPATA5L1	2.784026	0.019933	Q99417	MYCBP	-2.93416	0.00531
P25815	S100P	3.271022	0.033728	P03928	URS00008BFBCB1	-2.91518	0.035965
Q96HF1	SFRP2	4.070217	0.018406	P02008	HBZ	-2.82732	0.044636
P31025	LCN1	4.304934	0.00327	P11166	SLC2A1	-2.81799	0.017834

**Table 3.** Top 10 DEPs in necrotic region between BME group and non-BME group.

Up-regulated DEPs				Down-regulated DEPs			
ID	Gene name	LogFC	Pvalue	ID	Gene name	LogFC	Pvalue
P01854	IGHE	3.903696	0.022994	A075B6	IGLV8-61	-4.5851	0.018539
P02749	APOH	3.949444	0.002297	P02008	HBZ	-4.19484	0.030112
P01909	HLA-DQA1	3.967956	0.022775	Q13103	SPP2	-3.65746	0.002659
Q86VB7	CD163	3.986324	0.00047	P18577	RHCE	-3.54882	0.03932
Q5SYB0	FRMPD1	4.139878	0.000686	P02655	APOC2	-3.21748	0.030157
P02745	C1QA	4.230826	0.001083	P41159	LEP	-3.1534	0.032841
Q86YA3	ZGRF1	4.595948	0.005517	Q8TDP1	RNASEH2C	-2.77697	0.016107
P01871	IGHM	4.641303	0.005578	Q10588	BST1	-2.58696	0.013768
P01859	IGHG2	5.234833	0.001806	P12259	F5	-2.43757	0.006304
Q9Y244	POMP	14.29266	0.041761	P05121	SERPINE1	-2.41973	0.010812

**Table 4.** Top 10 DEPs in sclerotic region between BME group and non-BME group.

group (Fig. 6C). This observation implies that individuals with BME may undergo heightened oxidative stress, consistent with the functional enrichment analysis results of the aforementioned DEPs.

To gain insights into the disparities in osteoclast activity and oxidative stress reactions between the two groups, we conducted a Western blot analysis to assess protein expression within the bone tissue. Our findings indicated that the expression levels of SOD-1 were notably diminished in the femoral neck, necrotic, and sclerotic areas of the BME group when compared to the control group. Furthermore, the expression of CTSK and RANKL was significantly elevated in the necrotic and sclerotic regions of the BME group relative to the control group, as illustrated in Fig. 6D-E.

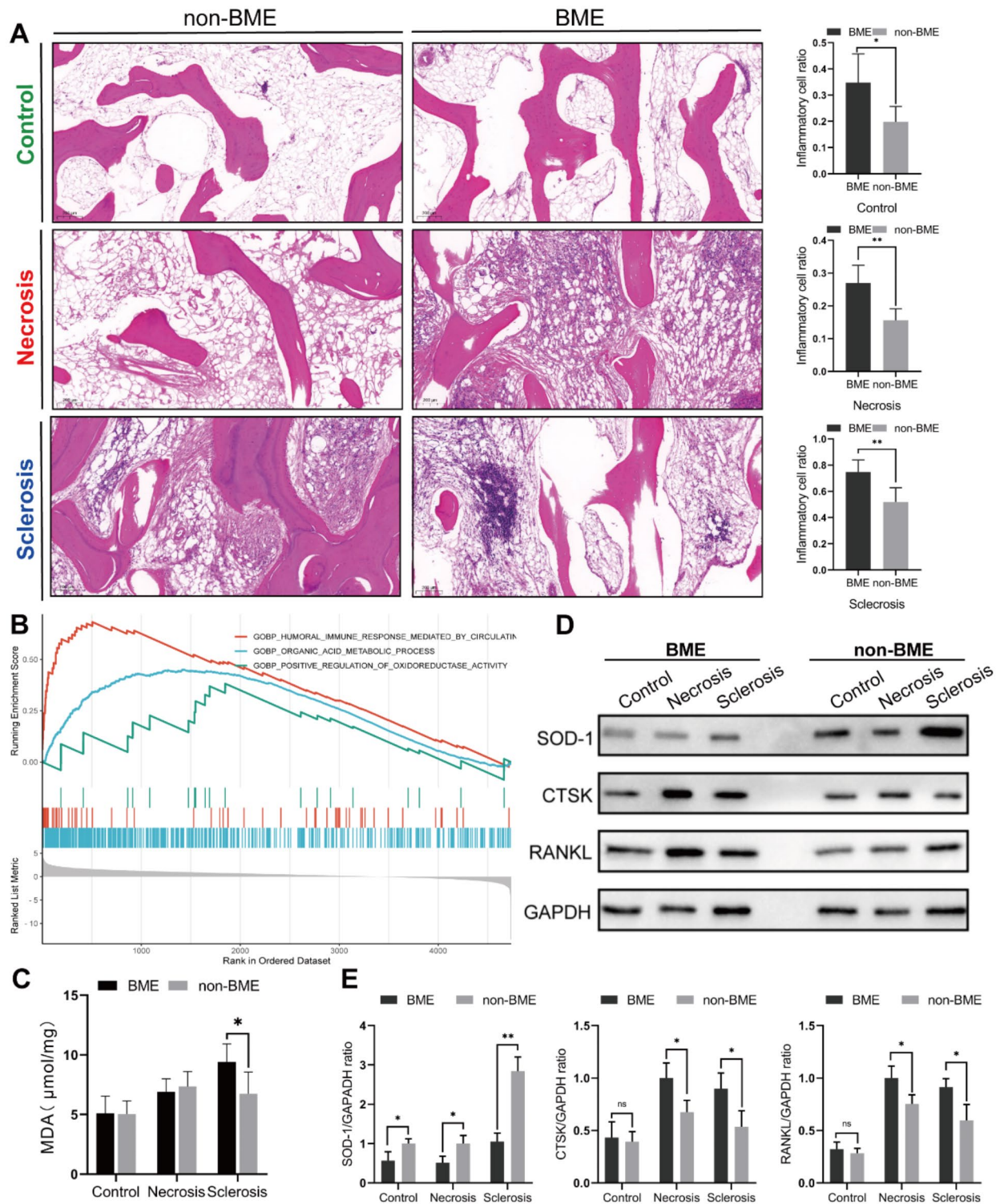


**Fig. 6.** Results of inflammatory cells quantitation, MDA testing and western blot analysis. **(A)** Representative images and inflammatory cell quantification in the control, necrotic and sclerotic regions. Scale bar = 200 μm. **(B)** Results of GSEA enrichment analysis of overall expressed proteins in the sclerotic region between BME group and non-BME group. **(C)** Bone tissue MDA detection results in the BME group and non-BME group.  $n = 5$  for each group. **(D-E)** Representative images and quantitation of western blot analysis, normalized to GAPDH.  $n = 3$  for each group. All bar graphs were presented as mean  $\pm$  SD ( $n = 3$ ). \* $p < 0.05$ , \*\* $p < 0.01$ .

## Discussion

Various clinical investigations have delved into the causes, mechanisms, and clinical consequences of BME in ONFH. Nevertheless, the precise pathological processes leading to femoral head collapse in ONFH cases with BME are still under discussion. Considering the substantial impact of BME on ONFH, this research endeavor was designed to illuminate the pathomechanisms of ONFH with BME during the peri-collapse period. For this purpose, we collected femoral head samples from patients at the peri-collapse stage, both with and without BME, who were undergoing THA. These samples underwent histomorphometric and histopathological analyses to evaluate differences between the BME and non-BME groups. Furthermore, we applied a DIA high-throughput proteomics approach to decipher the molecular foundations of disease progression in the femoral neck, necrotic, and sclerotic areas affected by BME. Insights gained from these analyses could provide a deeper understanding of the pathophysiology behind femoral head collapse in ONFH cases with BME, potentially guiding future therapeutic strategies.

The microstructure of bone is closely associated with the mechanical strength of the femoral head. Previous study has indicated that the early stage of ONFH does not exhibit significant changes in the appearance of the femoral head. However, there are already alterations in osteoblast and osteoclast activities within the subchondral bone and necrotic regions<sup>17</sup>. As a result of excessive bone resorption activity in the necrotic region and increased bone formation activity in the sclerotic region, the mechanical properties and structure of trabecular bone undergo significant changes<sup>18</sup>. In conjunction with sustained load pressure and stress, the subchondral trabecular bone eventually develops numerous microfractures when the applied pressure exceeds the load-bearing capacity of the trabeculae<sup>19</sup>. In the present study, we discovered that when ONFH is accompanied by severe BME, despite the absence of significant changes in the appearance of the femoral head, evident subchondral fractures can be observed on CT images. Patients with BME showed a high probability of low-density changes in CT. In addition, the expression levels of RANK and CTSK, which are bone resorption-related genes, were also increased in the BME group, especially in the necrotic and sclerotic regions. In a murine model of collagen-induced arthritis with subchondral BME, researchers observed significant changes in the bone marrow microenvironment following the onset of BME, including a notable increase in the number of osteoclasts and elevated expression of RANKL protein, increased proinflammatory cytokines and chemokines, and highly activated T cells and monocytes<sup>20</sup>. The results were consistent with our findings. Therefore, it is speculated that when ONFH is accompanied by BME, the enhanced activity of osteoclasts leads to increased bone resorption, resulting in a decline in the biomechanical properties of the bone tissue, which may be a contributing factor to the occurrence of femoral head collapse or re-collapse.

In this study, the rate of empty lacunae in the necrotic area was significantly higher in both the BME and non-BME groups when compared to the sclerotic and control bone tissues. Interestingly, there were no significant differences in the empty lacunae rate between the BME and non-BME groups in the control and sclerotic regions, suggesting that BME does not represent a direct extension of bone tissue necrosis. Additionally, DIA proteomics technique was used to identify DEPs between BME and non-BME groups. In total, 141, 299 and 853 DEPs were identified in the control, necrotic, and sclerotic regions, respectively. Notably, BME had the most significant impact on protein expression in the sclerotic region, with the most DEPs being upregulated. This observation might be attributed to BME in ONFH patients potentially serving as a secondary, reparative response to the ischemic tissue surrounding the necrotic area.

Enrichment analysis indicated that most enriched canonical pathways of DEPs in control, necrotic, and sclerotic regions encompassed immune, inflammation and oxidative stress related pathways, metabolic pathway, complement and coagulation cascades. Previous research has indeed identified chronic inflammation as a prominent feature of ONFH<sup>21</sup>. Tan et al. indicated that an imbalance between M1 and M2 macrophages promotes the progression of non-traumatic ONFH, which is a chronic inflammatory disease characterized by persistent inflammation, cell death, and tissue fibrosis in the affected area<sup>22</sup>. A porcine model demonstrated that necrotic bone byproducts can induce the upregulation of pro-inflammatory cytokines, a process dependent on macrophage activation of Toll-like Receptor 4<sup>23</sup>. This observation was replicated in a rat model of steroid-associated ONFH, revealing excessive TLR4/NF- $\kappa$ B activation and suppressed canonical Wnt/ $\beta$ -catenin pathway<sup>24</sup>. These studies indicated a close association between chronic inflammation and the progression of ONFH. Particularly, there is a higher degree of inflammatory cell infiltration in the sclerotic region. Moreover, inflammatory cytokines play a crucial role in recruiting endothelial cells, fibroblasts, and other tissue-regenerating cells to the sites of injury. These recruited cells contribute to the formation of blood vessels and the production of collagen, which ultimately results in the expansion of the extracellular matrix<sup>25</sup>. This process is closely associated with the development of fibrosis. Interestingly, we found that the expression levels of osteoclast related genes were also upregulated and more tissue fibrosis in the BME group. Therefore, we hypothesized that BME activates inflammatory responses, which further stimulate the activity of osteoclasts and enhance tissue fibrosis. And this could be one of the factors contributing to the accelerated progression of ONFH with BME.

Accumulated evidence indicated that oxidative stress was closely related to the process of ONFH<sup>26,27</sup>. In our previous study, reactive oxygen species (ROS)-related enzymes and osteoclasts were detected in both patients' ONFH specimens and rodent models mimicking ONFH, and the results revealed that the high oxidative stress may result from decreased expression of antioxidant enzymes, eventually leading to osteoclast hyperactivity and subsequently ONFH progression<sup>28</sup>. Notably, in this study, we observed a significant downregulation of superoxide dismutase1 (SOD1), an important antioxidant enzyme, in the BME group. This indicated a decrease in the capacity to scavenge ROS and counteract oxidative stress. Furthermore, we found that the levels of malondialdehyde (MDA), a marker for oxidative stress, were significantly increased in the sclerotic regions with BME compared to the control group. These findings suggested that there is an imbalance between antioxidant defense mechanisms and oxidative stress in ONFH individuals with BME, potentially contributing to the progression of the condition.

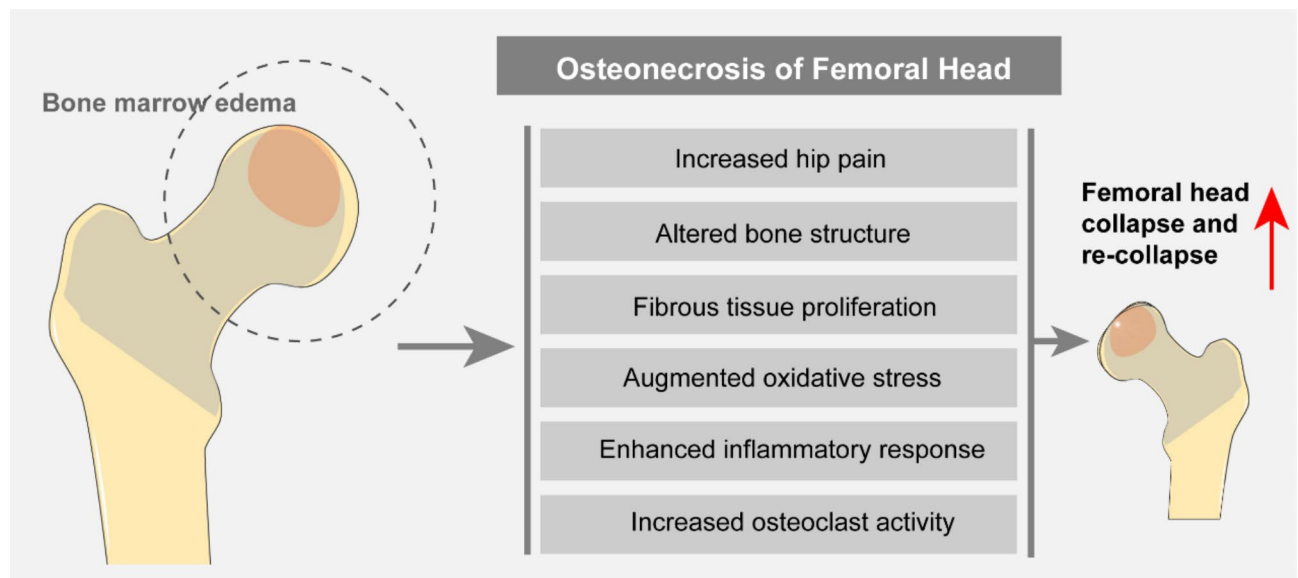


**Fig. 7.** A proposed scheme for the increased risks of femoral head collapse and re-collapse with BME in ONFH.

Metabolic pathway including carbon metabolism and acid catabolic process were significantly enriched in the DEPs, and these pathways were related to the cartilage and subchondral bone nutrient supply. Intriguingly enough, levels of most proteins engaged in nutrient metabolism were significantly up-regulated in the sclerotic region of ONFH patients with BME. The metabolic change may be the adaptation of ONFH bone tissue under BME conditions. Complement and coagulation cascade molecules and blood microparticle were identified in bone tissues with BME, which reveals that they are involved in the development of BME in patients with ONFH. Similar changes were also observed in the transcription analysis of bone tissue and the proteome analysis of cartilage in patients with ONFH<sup>29,30</sup>. Further investigation is expected about how these pathways are involved in the development of ONFH.

This study has certain limitations. Firstly, owing to the challenge of acquiring femoral head specimens from patients with extensive BME, only five specimens could be included in each group. To reach more solid conclusions, future studies should endeavor to increase the sample quantities. Secondly, given the inherently self-limiting nature of BME, this cross-sectional research cannot rule out the presence of pre-existing BME in the non-BME group. Thirdly, despite rigorous enforcement of baseline controls, there may still be individual differences among patients.

## Conclusion

BME in ONFH patients significantly impacts both the biological and morphological aspects of the surrounding environment. Biologically, the condition triggers inflammatory and oxidative stress responses, leading to tissue fibrosis and heightened osteoclast activity. This elevated osteoclast activity subsequently causes structural damage to the bone tissue. Morphologically, the primary change observed is an increase in the area of low bone mass. Such changes render the femoral head more prone to subchondral fractures under stress (Fig. 7).

## Data availability

The mass spectrometry proteomics data have been deposited to the ProteomeXchange Consortium (<https://proteomecentral.proteomexchange.org>) via the iProX partner repository with the dataset identifier PXD048708.

Received: 4 January 2024; Accepted: 13 December 2024

Published online: 07 January 2025

## References

- Sodhi, N. et al. Management of osteonecrosis of the femoral head. *bone joint J.* **102-B** (7\_Supple\_B), 122–128 (2020).
- Chen, Y. et al. Evolutionary course of the femoral head osteonecrosis: Histopathological - radiologic characteristics and clinical staging systems. *J. Orthop. Translat.* **32**, 28–40 (2022).
- Min, B. W. et al. Highly Cross-Linked Polyethylene in Total Hip Arthroplasty in Patients Younger Than 50 Years With Osteonecrosis of the Femoral Head: A Minimum of 10 Years of Follow-Up. *J. Arthroplast.* **35** (3), 805–810 (2020).
- Mo, L. et al. Influence of less invasive hip preservation surgery on subsequent hip arthroplasty for osteonecrosis of the femoral head. *J. Hip Preserv Surg.* **9** (3), 197–205 (2022).
- Chen, L. et al. Optimizing indications of impacting bone allograft transplantation in osteonecrosis of the femoral head. *bone joint J.* **102-B** (7), 838–844 (2020).
- Li, J. et al. One in five patients require conversion to arthroplasty after non-vascularized bone grafts in patients with osteonecrosis of the femoral head: a systematic review. *J. Orthop. Surg. Res.* **18** (1), 77 (2023).

7. Zhang, Q. Y., Li, Z. R., Gao, F. Q. & Sun, W. Pericollapse Stage of Osteonecrosis of the Femoral Head: A Last Chance for Joint Preservation. *Chin. Med. J.* **131** (21), 2589–2598 (2018).
8. Di Martino, A. et al. Bone marrow edema of the hip: a narrative review. *Arch. Orthop. Trauma Surg.* (2023).
9. Ito, H., Matsuno, T. & Minami, A. Relationship between bone marrow edema and development of symptoms in patients with osteonecrosis of the femoral head. *AJR Am. J. Roentgenol.* **186** (6), 1761–1770 (2006).
10. Meier, R. et al. Bone marrow oedema on MR imaging indicates ARCO stage 3 disease in patients with AVN of the femoral head. *Eur. Radiol.* **24** (9), 2271–2278 (2014).
11. Theruvath, A. J. et al. Bone marrow oedema predicts bone collapse in paediatric and adolescent leukaemia patients with corticosteroid-induced osteonecrosis. *Eur. Radiol.* **28** (1), 410–417 (2018).
12. Yoon, B. H. et al. The 2019 Revised Version of Association Research Circulation Osseous Staging System of Osteonecrosis of the Femoral Head. *J. Arthroplast.* **35** (4), 933–940 (2020).
13. Yang, Z., Shen, X., Chen, D. & Sun, L. Toward a Universal Sample Preparation Method for Denaturing Top-Down Proteomics of Complex Proteomes. *J. Proteome Res.* **19** (8), 3315–3325 (2020).
14. Choi, M. et al. MSstats: an R package for statistical analysis of quantitative mass spectrometry-based proteomic experiments. *Bioinformatics* **30** (17), 2524–2526 (2014).
15. Ma, J. et al. iProX: an integrated proteome resource. *Nucleic Acids Res.* **47** (D1), D1211–D1217 (2019).
16. Chen, T. et al. iProX in 2021: connecting proteomics data sharing with big data. *Nucleic Acids Res.* **50** (D1), D1522–D1527 (2022).
17. Wang, C. et al. Analysis of early stage osteonecrosis of the human femoral head and the mechanism of femoral head collapse. *Int. J. Biol. Sci.* **14** (2), 156–164 (2018).
18. Cao, H. J. et al. Src blockage by siRNA inhibits VEGF-induced vascular hyperpermeability and osteoclast activity - an in vitro mechanism study for preventing destructive repair of osteonecrosis. *Bone* **74**, 58–68 (2015).
19. Kim, H. K., Aruwajoye, O., Du, J. & Kamiya, N. Local administration of bone morphogenetic protein-2 and bisphosphonate during non-weight-bearing treatment of ischemic osteonecrosis of the femoral head: an experimental investigation in immature pigs. *J. bone joint Surg. Am.* **96** (18), 1515–1524 (volume 2014).
20. Wang, F. et al. The Bone Marrow Edema Links to an Osteoclastic Environment and Precedes Synovitis During the Development of Collagen Induced Arthritis. *Front. Immunol.* **10**, (2019).
21. Goodman, S. B. & Maruyama, M. Inflammation, Bone Healing and Osteonecrosis: From Bedside to Bench. *J. Inflamm. Res.* **13**, 913–923 (2020).
22. Tan, Z. et al. The Dynamic Feature of Macrophage M1/M2 Imbalance Facilitates the Progression of Non-Traumatic Osteonecrosis of the Femoral Head. *Front. Bioeng. Biotechnol.* **10**, 912133 (2022).
23. Adapala, N. S., Yamaguchi, R., Phipps, M., Aruwajoye, O. & Kim, H. K. W. Necrotic Bone Stimulates Proinflammatory Responses in Macrophages through the Activation of Toll-Like Receptor 4. *Am. J. Pathol.* **186** (11), 2987–2999 (2016).
24. Pei, J. et al. Excessive Activation of TLR4/NF-kappaB Interactively Suppresses the Canonical Wnt/beta-catenin Pathway and Induces SANFH in SD Rats. *Sci. Rep.* **7** (1), 11928 (2017).
25. Zhang, W.-J., Chen, S.-J., Zhou, S.-C., Wu, S.-Z. & Wang, H. Inflammasomes and Fibrosis. *Front. Immunol.* **12**, (2021).
26. Fan, Z. Q. et al. Oxidative Stress Induced Osteocyte Apoptosis in Steroid-Induced Femoral Head Necrosis. *Orthop. Surg.* **13** (7), 2145–2152 (2021).
27. Ichiseki, T. et al. Osteonecrosis development in a novel rat model characterized by a single application of oxidative stress. *Arthritis Rheum.* **63** (7), 2138–2141 (2011).
28. Chen, K. et al. Steroid-induced osteonecrosis of the femoral head reveals enhanced reactive oxygen species and hyperactive osteoclasts. *Int. J. Biol. Sci.* **16** (11), 1888–1900 (2020).
29. Luo, H. et al. Microarray analysis of long-noncoding RNAs and mRNA expression profiles in human steroid-induced avascular necrosis of the femoral head. *J. Cell. Biochem.* **120** (9), 15800–15813 (2019).
30. Song, J. et al. Proteomics analysis of hip articular cartilage identifies differentially expressed proteins associated with osteonecrosis of the femoral head. *Osteoarthr. Cartil.* **29** (7), 1081–1092 (2021).

## Acknowledgements

We thank Prof. Stuart B. Goodman from Stanford University for his constructive suggestions, and Lingnan Medical Research Center of Guangzhou University of Chinese Medicine for helpful technical support.

## Author contributions

Liang Mo and Zhangzheng Wang contributed equally to this article. Yuhao Liu, Zhenqiu Chen and Wei He supervised this research and contributed to sponsors. Liang Mo and Zhangzheng Wang performed the data analysis, designed the experimental validation. Mengyu Jiang, Chao Ma and Yinuo Fan carried out parts of the experiments and performed the DIA analysis. Chi Zhou participated in biospecimen collection. Liang Mo drafted the manuscript, and Yuhao Liu revised it. All authors approved the final manuscript.

## Declarations

## Competing interests

The authors declare no competing interests.

## Funding

This research was sponsored by Guangzhou Science and Technology Bureau (Grant No. 2024A04J9998), National Natural Science Foundation of China (Grant No. 82104883), Guangzhou Association for Science and Technology (Grant No. QT-2024-033), the First Affiliated Hospital of Guangzhou University of Chinese Medicine (Grant No. ZYYY2023-186 and ZYYY2024-87), Department of Science and Technology of Guangdong Province (Grant No. YKZZ2024–205 and 2022A1515011379) and Guangzhou Municipal Health Commission (Grant No. 2023P-TS22).

## Consent for publication

All authors have agreed to the content of the manuscript and agree to this submission.

## Ethics approval and consent to participate

This study was approved by the Ethical Committee of the First Affiliated Hospital of Guangzhou University

of Chinese Medicine (No. K-2022-059). All patients provided written informed consent to participate in this research.

### Additional information

**Supplementary Information** The online version contains supplementary material available at <https://doi.org/10.1038/s41598-024-83376-6>.

**Correspondence** and requests for materials should be addressed to W.H., Z.C. or Y.L.

**Reprints and permissions information** is available at [www.nature.com/reprints](http://www.nature.com/reprints).

**Publisher's note** Springer Nature remains neutral with regard to jurisdictional claims in published maps and institutional affiliations.

**Open Access** This article is licensed under a Creative Commons Attribution-NonCommercial-NoDerivatives 4.0 International License, which permits any non-commercial use, sharing, distribution and reproduction in any medium or format, as long as you give appropriate credit to the original author(s) and the source, provide a link to the Creative Commons licence, and indicate if you modified the licensed material. You do not have permission under this licence to share adapted material derived from this article or parts of it. The images or other third party material in this article are included in the article's Creative Commons licence, unless indicated otherwise in a credit line to the material. If material is not included in the article's Creative Commons licence and your intended use is not permitted by statutory regulation or exceeds the permitted use, you will need to obtain permission directly from the copyright holder. To view a copy of this licence, visit <http://creativecommons.org/licenses/by-nc-nd/4.0/>.

© The Author(s) 2025